Uncovering the deformation mechanisms of origami metamaterials by introducing generic degree-four vertices

Hongbin Fang, Suyi Li, Huimin Ji, and K. W. Wang

Phys. Rev. E **94**, 043002 — Published 24 October 2016

DOI: 10.1103/PhysRevE.94.043002

Uncovering the deformation mechanisms of origami metamaterials by introducing generic degree-4 vertices

Hongbin Fang[1*], Suyi Li[2], Huimin Ji[1] and K.W. Wang[1]

1) Department of Mechanical Engineering, University of Michigan, Ann Arbor, MI 48109, USA
2) Department of Mechanical Engineering, Clemson University, Clemson, SC 29634, USA

[*]**Corresponding author:** hongbinf@umich.edu

Abstract:

Origami-based design holds promise for developing new mechanical metamaterial whose overall kinematic and mechanical properties can be programmed using purely geometric criteria. In this article, we demonstrate, for the first time, that the deformation of a generic degree-4 vertex (4-vertex) origami cell is a combination of contracting, shearing, bending, and facet-binding. The last three deformation mechanisms are missing in the current rigid-origami metamaterial investigations of which focuses were mainly on conventional Miura-ori patterns. We show that these mechanisms provide the 4-vertex origami sheets and blocks with new deformation patterns as well as extraordinary kinematical and mechanical properties, including self-locking, tri-directional negative Poisson's ratios, flipping of stiffness profiles, and emerging shearing stiffness. This study reveals that the 4-vertex cells offer a better platform and greater design space for developing origami-based mechanical metamaterials than the conventional Miura-ori cell.

I. INTRODUCTION

One of the recent interests in origami research is to translate the principles of paper folding into the designs of novel mechanical metamaterials [1–8]. Such metamaterials are essentially periodic assemblies of origami units so that their overall unusual mechanical properties are defined by the intricate folding geometry rather than the constituent materials. Auxetic effects [1,2,5], nonlinear stiffness [2–4,9], and multistability [5,7,10–14] have been reported. These unorthodox properties are programmable via synthesizing the folding crease pattern; combined with the foldability and scalability of origami, they offer the origami-based mechanical metamaterials with promising application potentials [15–18].

The aforementioned properties of origami metamaterials mainly originate from the kinematics of rigid-folding. Rigid-foldable origami retains one degree-of-freedom for folding even if its facets are assumed to be rigid panels connected by perfect hinges. The most elementary rigid-foldable unit for building origami metamaterials is the degree-4 vertex (for short, 4-vertex) [19], which consists of four rigid sectors connected by four folds that meet at a point. The current state of the art in rigid-origami metamaterials is mainly based on a very special 4-vertex: the Miura-ori and its close relatives [1,2,4,5,8]. Miura-ori design is constrained by two conditions: one is being flat-foldable that the origami can be folded to a flat state; and the other is having two collinear crease lines. Such strong constraints simplify the geometry but limit the deformation of Miura-based metamaterials to contraction and extension only. On the other hand, several recent studies systematically investigated the folding kinematics and multi-stability of 4-vertices [13,19], which illustrates the potentials of extending the metamaterial research from Miura-ori to generic 4-vertices.

Here we present a framework of translating the folding kinematics of the constituent generic 4-vertex to the deformation mechanisms and mechanical properties of the overall origami metamaterial. Specifically, we demonstrate that the deformation of a generic 4-vertex origami cell is a combination of in-plane and out-of-plane shearing, bending, contracting, and facet-binding; the first two have not been discovered in rigid-origami metamaterials before. We show that these deformation mechanisms are partially passed down to three types of non-generic 4-vertex cell: general flat-foldable, single collinear, and Miura-ori cells. Furthermore, we show that the newly discovered deformation mechanisms of the constituent cell provide the origami sheets and stacked blocks with extraordinary properties that are unseen from previous studies. In terms of kinematics, the design space for constructing metamaterial is significantly expanded by introducing rich and new deformations patterns and large ranges of achievable maximum deformation. In terms of mechanical properties, the shear deformations can induce tri-directional negative Poisson's ratio and can qualitatively alter the stiffness profiles (including generating shearing stiffness). It's worth noting that while the focus of this study is on metamaterials, the approach is fundamental and generic, and thus the outcome will advance and impact the overall field of origami research.

II. GEOMETRIES AND DEFORMATION MECHANISMS

We start with a generic 4-vertex (G-4) cell without any geometry constraints. It consists of four rigid parallelogram facets connected by four folds; its geometry is characterized by two length parameters (a, b) and four sector angles α_i ($i=1,2,3,4$) (see Fig. 1(a)). Assuming that $\sum\alpha_i = 360^\circ$ and $\alpha_j < \sum\alpha_{i\neq j}$ to avoid triviality [19], there are three independent sector angles (say, α_1, α_2 and α_4). A partially folded state of the cell is described by the dihedral angles ρ_i between adjacent facets ($\rho_i \in (0^\circ,180^\circ)$ for "mountain", $\rho_i \in (180^\circ,360^\circ)$ for "valley", $\rho_i = 180^\circ$ for unfolded state, and $\rho_i = 0^\circ$ or 360° for fully-folded state). To describe its deformation, four auxiliary planes (I to IV) are constructed (Fig. 1(b)). In this research, to facilitate the study on cell deformation, without loss of generality, we assume that α_1 is the smallest sector angle, fold 4 has the opposite type (say, "valley" fold) from the rest (i.e., ρ_4 is the unique fold, which calls for $\alpha_1+\alpha_4<\pi$ [19]), and fold 1 is capable of fully closing to 0° (i.e., ρ_1 is the binding fold).

We categorize the 4-vertex cells into 4 types based on whether the cell possess flat-foldability ($\alpha_1+\alpha_3=\alpha_2+\alpha_4$) or single-collinearity ($\alpha_1+\alpha_2=\alpha_3+\alpha_4$). The G-4 cell cannot be folded flat nor has collinear creases; the general flat-foldable (GFF) cell possesses flat-foldability; the single-collinear (SC) cell has a pair of collinear creases; and the Miura-ori cell has both characters. For convenience, we assign α_1 and α_4 (for simplicity, denoted by α and β, respectively) as the independent angles of the GFF and SC cells, α_1 (denoted by α) as the independent angle of the Miura-ori cell (Fig. 1(a)).

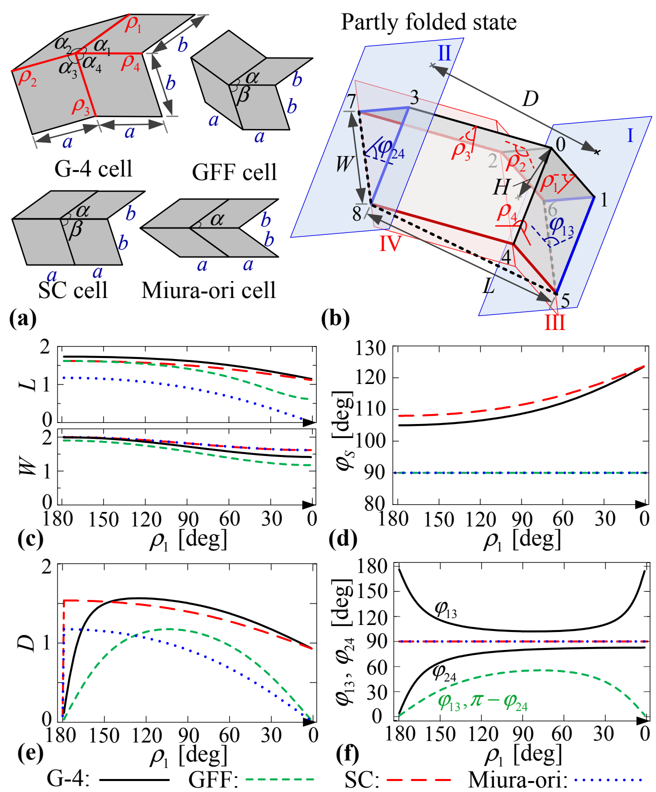

FIG. 1. Geometries and deformations of 4-vertex origami cells. (a) Initial flat states of a G-4 cell and three non-generic cells. (b) Partly folded state of a G-4 cell, where each auxiliary plane is spanned by two edges, namely, I (1-3, 1-4), II (3-7, 3-8), III (2-6, 4-5), and IV (2-7, 4-8); height H is defined as the distance from vertex 0 to plane III. (c) L and W, (d) φ_s, (e) D, and (f) φ_{13} and φ_{24} as functions of ρ_1. For the four types of cell, the lengths a and b are set to be the same $a=b=1$. G-4 cell: $\alpha_1 = 36^\circ, \alpha_2 = 160^\circ, \alpha_4 = 72^\circ$; GFF and SC cells: $\alpha = 36^\circ, \beta = 72^\circ$; Miura-ori cell: $\alpha = 36^\circ$.

The following geometry quantities are defined to examine the cell deformation (Fig. 1(b)): the length L, width W, and height H of a cell; the angle φ_S between the length and width directions; the dihedral angles φ_{13} between the auxiliary planes I and III and φ_{24} between planes II and IV; and the distance D between planes I and II. Hence, changing of L and W indicates the contraction of a cell; φ_S is a measure of the possible in-plane shear of a cell; changing of φ_{13} and φ_{24} represents the out-of-plane shear of a cell; the relationship between φ_{13} and φ_{24} illustrates the relative bend of a cell; and D is used to quantify whether facet-binding happens at a non-flat state.

We calculate the above quantities for the four types of cell through vector operations (Appendix A). Fig. 1(c)-(f) show these quantities as a function of ρ_1, from the initial flat state $\rho_1 = 180^\circ$ to the fully-folded state $\rho_1 = 0^\circ$. For the G-4 cell, the following phenomena are observed: (1) L and W decrease with ρ_1, indicating the contraction of the cell; (2) φ_S changes with ρ_1, suggesting an in-plane shear; (3) φ_{13} and φ_{24} changes with ρ_1, revealing an out-of-plane shear; (4) φ_{13} is different from φ_{24} or $180^\circ - \varphi_{24}$, implying a relative bend between the left and right halves of the cell; (5) D does not return to zero when $\rho_1 = 0$, manifesting that the G-4 cell cannot be further folded to a flat state when ρ_1 fully closes, i.e., facet-binding happens at a non-flat state. In summary, the deformation of the G-4 cell is a combination of contracting, in-plane and out-of-plane shearing, bending, and facet-binding.

Fig. 1(c)~(f) also reveal that the abovementioned deformation mechanisms are partially passed down to the non-generic 4-vertex cells. The GFF cell inherits the contracting and out-of-plane shearing, but loses the in-plane shearing (φ_S keeps constant), bending (φ_{13} always equals to $\pi - \varphi_{24}$), and facet-binding (D returns zero); the SC cell inherits the contracting, in-plane shearing, and facet-binding, but loses the out-of-plane shearing and bending (φ_{13} and φ_{24} keep constant and identical); the most studied Miura-ori cell only inherits the contracting, which explains why the other deformation mechanisms have never been discovered in Miura-based metamaterials. Table I summarizes the deformation mechanisms of the four types of cell.

TABLE I. Deformation mechanisms of 4-vertex cells, sheets and blocks. "*c*" stands for contracting, "*i-s*" for in-plane shearing, "*o-s*" for out-of-plane shearing, "*b*" for bending, and "*f-b*" for facet-binding.

Types		*c*	*i-s*	*o-s*	*b*	*f-b*
G-4	cell	√	√	√	√	√
	sheet	√	√	√		√
GFF	cell and sheet	√		√		
	block	√		√		√
SC	cell and sheet	√	√			√
	block	√	√			√
Miura-ori	cell and sheet	√				
	block	√				

III. CONSTRUCTIONS OF 4-VERTEX ORIGAMI METAMATERIALS

The above uncovered deformation mechanisms motivate us to develop origami metamaterials with generic 4-vertices, and to explore their extraordinary properties. In this section, we introduce the construction of 4-vertex origami sheets and blocks. Taking the 4-vertex cell as a unit, origami sheets can be assembled by repeating identical cells along the L and W directions (see Fig. 2). Waitukaitis et al. [13] have pointed out that such tessellation would introduce three new vertices, namely, a rotated vertex, a "complementary vertex" with sector angles $\{\pi-\alpha_i\}$, and a rotated complementary vertex. However, these newly generated vertices remain the same type as the original vertex and do not change the folding kinematics of the original vertex (including the unique fold, the binding fold, and the binding angle) [13]. Hence, deformation mechanisms of the original vertex will not be affected, and the newly generated vertices will not acquire additional mechanisms or lose certain mechanisms.

Note that although the GFF and SC cells only inherit some of the deformation mechanisms from the G-4 cell due to the additional constraints on sector angle assignments, their geometries are much simplified and can be explicitly expressed (Appendix B). More importantly, through similar techniques as [1], it is feasible to further integrate two GFF or SC cells along their zig-zag crease lines into a stacked unit based on the following relationship (Appendix C):

$$b_{\mathrm{B}} = b_{\mathrm{A}},\ \frac{a_{\mathrm{B}}}{a_A} = \frac{\cos\alpha_{\mathrm{A}}}{\cos\alpha_{\mathrm{B}}},\ \frac{\cos\alpha_{\mathrm{A}}}{\cos\alpha_{\mathrm{B}}} = \frac{\cos\beta_{\mathrm{A}}}{\cos\beta_{\mathrm{B}}}, \tag{1}$$

where the subscripts 'A' and 'B' denote the bottom cell A and top cell B, respectively. Taking α_B as the independent variable of the top cell, and without loss of generality we let $\alpha_B \geq \alpha_A$ so that cell A can be either nested into or bulged out from cell B, corresponding to two topologically different stacked units (see Fig. 2). Folding of the stacked unit is still a one degree-of-freedom motion, because the folding angles of cell B can be uniquely determined by those of cell A. Repeating the stacked units in *L*, *W*, and *H* directions yield the corresponding GFF or SC stacked blocks. Note that Miura-ori cells can also be stacked up with degenerated stacking conditions [1]; but the G-4 cells are geometrically-incompatible to be stacked together due to the bending deformation.

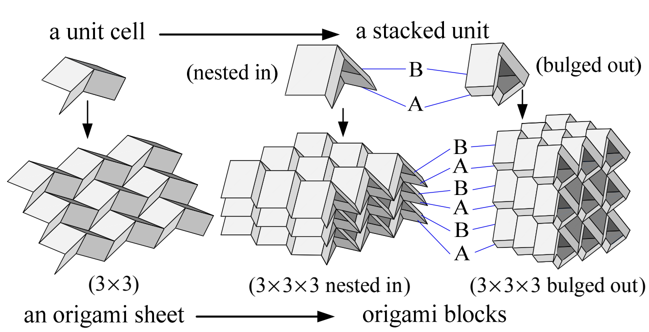

FIG. 2. Construction of origami sheets and blocks.

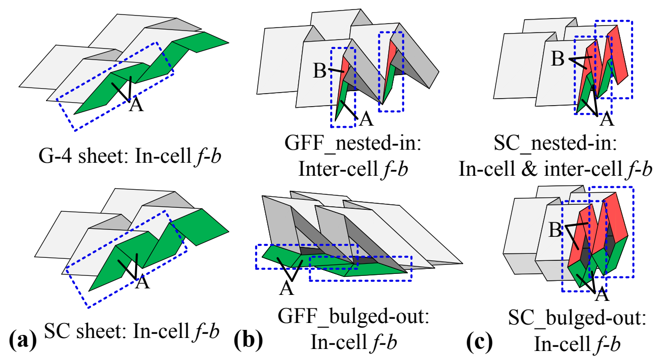

FIG. 3. Self-locking phenomena in (a) G-4 and SC sheets, (b) GFF block, and (c) SC block. The binding-facets are indicated by doted rectangles, and the corresponding self-locking mechanisms are denoted.

IV. KINEMATICS OF 4-VERTEX ORIGAMI METAMATERIALS

We now investigate how the newly discovered deformation mechanisms contribute to the kinematics of the 4-vertex sheets and blocks. We first point out that as component units, the 4-vertex cells' contracting, shearing, and facet-binding deformations can be accordingly passed on to the corresponding sheets. However, bending is lost when repeating the G-4 cell into G-4 sheet because the out-of-plane shear is counteracting the bending such that the planes I and II remain parallel during folding. Similarly, the contracting, shearing, and facet-binding are further passed on to the GFF, SC, and Miura-ori stacked blocks [21]. However, the GFF block is no longer flat-foldable and regains the facet-binding mechanism. Table I also displays the deformation mechanisms of the 4-vertex sheets and stacked blocks; video illustrations are given in Supplemental material [20].

Particularly, facet-binding will induce self-locking in certain 4-vertex sheets and stacked blocks, due to two different mechanisms: in-cell facet-binding and inter-cell facet-binding. We show that self-locking of the G-4 and SC sheets is due to in-cell facet-binding, i.e., two facets in each cell bind together to prevent the whole sheet from further folding (Fig. 3(a)). The GFF block has two self-locking states (Fig. 3(b)): self-locking in the nested-in configuration is attributed to inter-cell facet-binding, i.e., one facet of the top cell and one facet of the bottom cell in each stacked unit bind together, which prevents the whole block from further folding; self-locking in the bulged-out configuration is because the bottom cell is folded into a flat state and all the four facets bind together, which is still the effect of in-cell facet-binding. The SC block also has two self-locking states (Fig. 3(c)): self-locking in the nested-in configuration is due to a combined action of the two mechanisms; self-locking in the bulged-out configuration is induced by two separate in-cell facet-bindings. See detailed analysis in Appendix D. Note that while [1] provided an example of self-locking, here we present a generic and basic mechanism analysis.

Moreover, we demonstrate that the GFF and SC sheets/blocks feature larger ranges of maximum achievable deformation than the previously investigated Miura-ori design. In length and width directions, we examine the maximum achievable strains, defined as

$$\hat{\varepsilon}_L := (L_f - L_0)/L_0, \quad \hat{\varepsilon}_W := (W_f - W_0)/W_0, \tag{2}$$

where L_0 and W_0 are the initial length and width of the sheet/block, respectively; L_f and W_f are the final length and width of the sheet/block when the binding fold is fully folded, respectively. Moreover, we examine $\Delta\hat{\varphi}_{13} := (\varphi_{13})_{\max} - (\varphi_{13})_{\min}$ in GFF sheets/blocks to reveal the maximum achievable out-of-plane shearing deformation, and $\Delta\hat{\varphi}_S := (\varphi_S)_{\max} - (\varphi_S)_{\min}$ in SC sheets/blocks to manifest the maximum achievable in-plane shearing deformation[1]. These quantities are evaluated in the whole design space, shown in Fig. 4. Considering the assumptions that $\alpha_1 = \alpha$ is the smallest sector angle, and ρ_4 is the unique fold, only the variable range surrounded by $\alpha = \beta$, $\alpha + \beta = 180^\circ$, and $0 < \alpha < 90^\circ$ is studied.

For both cases, the Miura-ori design locates just on the dotted line $\alpha = \beta$. Figure 4 reveals that in the length and width directions, the maximum achievable strain of the Miura-ori sheet/block is programmable only in the length direction, while fixed at 100% in the width direction regardless of the value of α. However, the maximum achievable strains of the GFF/SC sheet/block can be programmed in both the length and width directions from 0 to 100%. Moreover, the Miura-ori sheet/block does not possess shearing deformability ($\Delta\hat{\varphi}_{13} \equiv 90^\circ$ and $\Delta\hat{\varphi}_S \equiv 0$). Nevertheless, the GFF designs could reach any out-of-plane shearing deformation between $\Delta\hat{\varphi}_{13} = 0^\circ$ and $\Delta\hat{\varphi}_{13} = 90^\circ$; and the SC designs could reach any in-plane shearing deformation between $\Delta\hat{\varphi}_S = 0$ and $\Delta\hat{\varphi}_S \approx 60^\circ$. Such enlargement of the maximum achievable deformation ranges is beneficial to the development of origami metamaterials.

[1] The subscript "max" and "min" indicate the maximum and minimum value of the angle during the whole folding process.

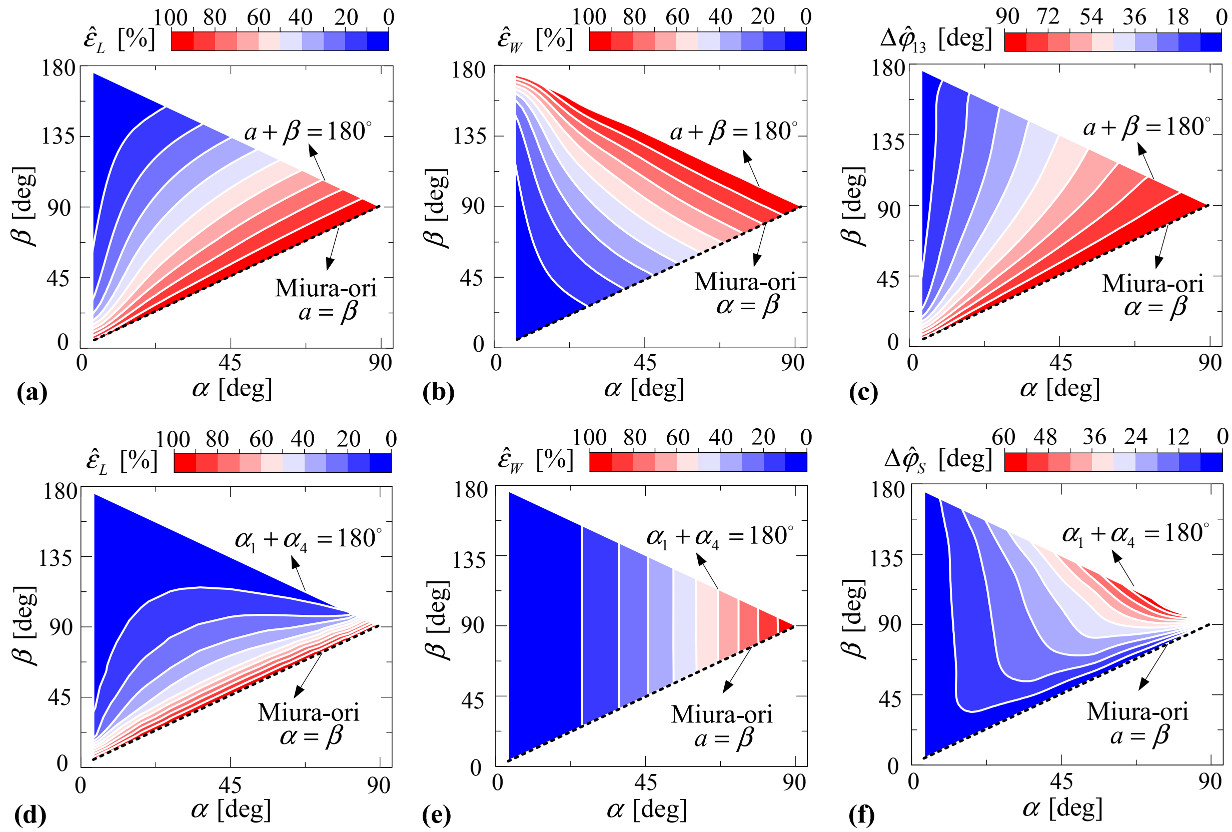

FIG. 4. Maximum achievable deformations of the GFF and SC sheet/block. (a)~(c) correspond to $\hat{\varepsilon}_L$, $\hat{\varepsilon}_W$, and $\Delta\hat{\varphi}_{13}$ in GFF design, respectively; (d)~(f) correspond to $\hat{\varepsilon}_L$, $\hat{\varepsilon}_W$, and $\Delta\hat{\varphi}_S$ in SC design, respectively. The Miura-ori design locates on the dashed lines $\alpha=\beta$.

V. MECHANICS OF 4-VERTEX ORIGAMI METAMATERIALS

We now discuss the mechanical properties of the 4-vertex sheets and blocks. We first focus on the Poisson's ratios of the GFF, SC and Miura-ori sheets, which can be calculated as

$$\nu_{HL}=-\frac{\mathrm{d}H/H}{\mathrm{d}L/L},\ \nu_{WL}=-\frac{\mathrm{d}W/W}{\mathrm{d}L/L}. \tag{3}$$

Fig. 5 displays the values of ν_{HL} and ν_{WL} with respect to ρ_1. For the SC and Miura-ori sheets, ν_{HL} remains positive, and ν_{WL} remains negative during the whole folding process. However, for the GFF sheet, although ν_{WL} still keeps negative, ν_{HL} experiences a flip from positive to negative due to the out-of-plane shear. Hence, there exists an interval in which the GFF sheet exhibits negative Poisson's ratio in three directions. Such tri-directional auxetic effects has been reported on Tachi-Miura polyhedron tubes [5] and stacked Miura blocks [1], but have never been discovered in single layer origami sheets. We also extend Poisson's ratio study to stacked blocks (Appendix E). We notice that similar flipping of Poisson's ratio is reserved in the bulged-out GFF block, but are lost in the nested-in configuration.

Then we discuss the effects of the new deformation mechanisms on the stiffness properties. In rigid origami, the elastic energy is stored only in the crease hinges which allow the rigid facets to rotate. Assigning k_0 as the linear torsional stiffness per unit length at each crease, the torsional spring constant (K_i) at each crease corresponding to the dihedral angle (ρ_i) can be calculated by multiplying k_0 with the crease length. The total spring energy of a 4-vertex cell with respect to the folding process is

$$\Pi = \frac{1}{2}\sum_{i=1}^{4} K_i\left(\rho_i - \rho_i^0\right)^2, \tag{4}$$

where ρ_i^0 is the initial dihedral angle corresponding to the initial stress free configuration (ρ_1^0). Then the tangent stiffness of the origami sheet can be determined via variation principle. The stretching stiffness in the length and height directions are given by $K_L = \mathrm{d}^2\Pi/\mathrm{d}L^2$ and $K_H = \mathrm{d}^2\Pi/\mathrm{d}H^2$, respectively. Particularly, due to the emerging shearing deformation, we also investigate the in-plane and out-of-plane shearing stiffness defined as $G_I = \mathrm{d}^2\Pi/\mathrm{d}\varphi_S{}^2$ and $G_O = \mathrm{d}^2\Pi/\mathrm{d}\varphi_{13}{}^2$, respectively. Stiffness of the staked blocks can be determined using similar arguments (Appendix F).

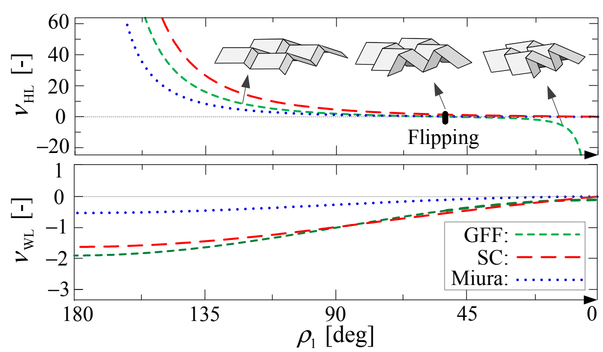

FIG. 5. Poisson's ratios ν_{HL} and ν_{WL} of the three types of sheet (with the same geometry parameters as those in Fig. 1). Insets illustrate the states of the 2×2 GFF sheets before, at, and after the flipping.

Fig. 6 displays the normalized stretching and shearing stiffness of the GFF, SC, and Miura sheets with respect to the folding process. The key observation is that the shearing deformation generates finite in-plane shearing stiffness G_I in the SC sheet (Fig. 6(c)) and finite out-of-plane shearing stiffness G_O in the GFF sheet (Fig. 6(d)). Such shearing stiffness has never been observed or reported on other types of rigid origami. Moreover, such shearing stiffness comes only from rigid-folding, indicating that the corresponding metamaterials are able to withstand shear deformation without bending or twisting of the facets or creases, which is significantly different with other shear behavior reported in [2,3] where facet/crease material deformation is a necessity. Note that due to the loss of corresponding shear deformation, the GFF and Miura-ori sheets cannot feature in-plane shearing stiffness from rigid-folding, and the SC and Miura-ori sheets cannot feature out-of-plane shearing stiffness either; in other words, they can bear shear deformation only if material deformation is allowed.

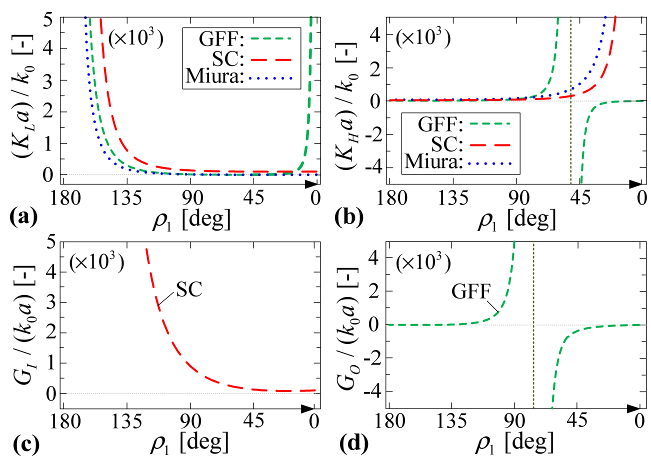

FIG. 6. Normalized stretching and shearing stiffness of the three types of sheet (with the same geometry parameters as those in Fig. 1): (a) $(K_L a)/k_0$, (b) $(K_H a)/k_0$, (c) $G_I/(k_0 a)$, and (d) $G_O/(k_0 a)$ as functions of ρ_1.

In addition, we see that the out-of-plane shearing deformation qualitatively alters the stiffness profiles in the GFF sheet. At the ending stage of folding, K_L undergoes a sudden increase (Fig. 6(a)) because the sheet is close to the flat state and the rate of length change is very small. We also observe a pair of stiffness jump and a stiffness switch on K_H and G_O (Fig. 6(b)); such discontinuity on stiffness is because H and φ_{13} experience switches from increase to decrease due to the out-of-plane shear (Appendix F).

VI. SUMMARY AND OUTLOOK

Our analysis on the deformation mechanisms and the resulting physical properties of the 4-vertex origami metamaterials are rooted in the geometry of the unit 4-vertex cells. Starting with the most generic 4-certex cell, the G-4 cell, we have illustrated that its deformation is a combination of contraction, in-plane and out-of-plane shearing, bending, and facet-binding. The last three mechanisms are missing in the current Miura-ori-based metamaterial research. These mechanisms could be partly inherited by the GFF, SC, and Miura-ori cells, which are generated by incorporating additional constraints among sector angles.

We have also established the relationship between the deformation mechanisms and the metamaterials' kinematic/mechanical properties. We find that by breaking the Miura-ori limitation, the GFF and SC designs can significantly expand their maximum available deformation ranges. Furthermore, the newly uncovered deformation mechanisms introduce various novel properties: facet-binding provides the metamaterials with self-locking ability, out-of-plane shear generates tri-directional negative Poisson's ratio in GFF designs, and in-plane and out-of-plane shears offer the metamaterials with shearing stiffness without material deformation.

Finally we would like to remark that this research paves the way for applying 4-vertex origami design into metamaterial development. Our analysis allows us to formulate and solve inverse design problems to derive the geometry parameters of the 4-vertex cell that lead to specified deformation patterns (ref. Table 1) and deformation capability (ref. Fig. 4).

ACKNOWLEDGEMENT

This research is supported by the University of Michigan Mechanical Engineering Collegiate Professorship.

Appendix A. Geometry quantities in vector space

Here we introduce the principles of calculating the geometry quantities L, W, H, φ_S, D, φ_{13}, φ_{24}, and θ_i $(i=1,2,3,4)$ in a 3D vector space. We first calculate the coordinates of each vertex in a cell (for clarity, vertex i in Fig. A1 is denoted by V_i $(i=0,\ldots,8)$). Based on spherical trigonometry, the dihedral angles ρ_i $(i=2,3,4)$ can be expressed as functions of ρ_1 [20]:

$$\begin{aligned}
\rho_2 &= \arccos\left(\frac{\cos\alpha_1-\cos\alpha_2\cos\xi}{\sin\alpha_2\sin\xi}\right)+\arccos\left(\frac{\cos\alpha_4-\cos\alpha\cos\xi}{\sin\alpha_3\sin\xi}\right),\\
\rho_3 &= \arccos\left(\frac{\cos\xi-\cos\alpha_3\cos\alpha_4}{\sin\alpha_3\sin\alpha_4}\right),\\
\rho_4 &= \arccos\left(\frac{\cos\alpha_2-\cos\alpha_1\cos\xi}{\sin\alpha_1\sin\xi}\right)+\arccos\left(\frac{\cos\alpha_3-\cos\alpha_4\cos\xi}{\sin\alpha_4\sin\xi}\right).
\end{aligned} \tag{A1}$$

where $\xi=\arccos(\cos\alpha_1\cos\alpha_2+\sin\alpha_1\sin\alpha_2\cos\rho_1)$. Considering the relative relations among folds (i.e., the dihedral angles ρ_i $(i=1,\ldots,4)$ and the sector angles α_i $(i=1,\ldots,4)$), coordinates of all vertices can be expressed in a certain rectangular coordinate system, with ρ_1 as the independent variable. Here, we use coordinate system $o-xyz$ shown in Fig. A1. With the obtained vertex coordinates, all vectors in the cell can be accordingly expressed, which facilitate the following-up calculations.

The length L and width W of a cell can be determined by

$$L=\left|\overrightarrow{\mathrm{V}_5\mathrm{V}_8}\right|,\quad W=\left|\overrightarrow{\mathrm{V}_7\mathrm{V}_8}\right|. \tag{A2}$$

The angle φ_S can be expressed as

$$\varphi_S=\arccos\frac{\overrightarrow{\mathrm{V}_5\mathrm{V}_8}\cdot\overrightarrow{\mathrm{V}_7\mathrm{V}_8}}{\left|\overrightarrow{\mathrm{V}_5\mathrm{V}_8}\right|\left|\overrightarrow{\mathrm{V}_7\mathrm{V}_8}\right|}. \tag{A3}$$

To obtain the other quantities, we first define the auxiliary planes. The plane I is spanned by $\overrightarrow{\mathrm{V}_1\mathrm{V}_6}$ and $\overrightarrow{\mathrm{V}_1\mathrm{V}_5}$; the plane II is spanned by $\overrightarrow{\mathrm{V}_3\mathrm{V}_7}$ and $\overrightarrow{\mathrm{V}_3\mathrm{V}_8}$; the plane III is spanned by $\overrightarrow{\mathrm{V}_6\mathrm{V}_2}$ and $\overrightarrow{\mathrm{V}_6\mathrm{V}_4}$; and the plane IV is spanned by $\overrightarrow{\mathrm{V}_7\mathrm{V}_2}$ and $\overrightarrow{\mathrm{V}_7\mathrm{V}_4}$. The normal vector of each auxiliary plane (denoted by $\overrightarrow{\mathrm{N}_{\mathrm{I}}}$ to $\overrightarrow{\mathrm{N}_{\mathrm{IV}}}$) can be calculated as

$$\begin{aligned}
&\overrightarrow{\mathrm{N}_{\mathrm{I}}}=\overrightarrow{\mathrm{V}_1\mathrm{V}_6}\times\overrightarrow{\mathrm{V}_1\mathrm{V}_5},\quad \overrightarrow{\mathrm{N}_{\mathrm{II}}}=\overrightarrow{\mathrm{V}_3\mathrm{V}_7}\times\overrightarrow{\mathrm{V}_3\mathrm{V}_8},\\
&\overrightarrow{\mathrm{N}_{\mathrm{III}}}=\overrightarrow{\mathrm{V}_6\mathrm{V}_2}\times\overrightarrow{\mathrm{V}_6\mathrm{V}_4},\quad \overrightarrow{\mathrm{N}_{\mathrm{IV}}}=\overrightarrow{\mathrm{V}_7\mathrm{V}_2}\times\overrightarrow{\mathrm{V}_7\mathrm{V}_4}.
\end{aligned} \tag{A4}$$

Then the height H yields

$$H=\frac{\left|\overrightarrow{\mathrm{V}_0\mathrm{V}_4}\cdot\overrightarrow{\mathrm{N}_{\mathrm{III}}}\right|}{\left|\overrightarrow{\mathrm{N}_{\mathrm{III}}}\right|}. \tag{A5}$$

The distance D between the planes I and III can be calculated via

$$D=\frac{\left|\overrightarrow{\mathrm{V}_3\mathrm{V}_1}\cdot\overrightarrow{\mathrm{N}_{\mathrm{I}}}\right|}{\left|\overrightarrow{\mathrm{N}_{\mathrm{I}}}\right|}. \tag{A6}$$

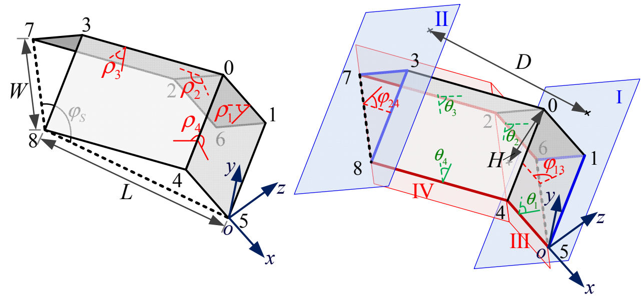

FIG. A1. A partly folded state of a 4-vertex cell in 3D vector space. The rectangular coordinate system $o-xyz$ is such built: the auxiliary plane III is assigned as the $x-o-y$ plane, the vertex V_5 is assigned as the origin, the x -axis extends along V_4V_5, the $y-$axis is determined by rotating the $x-$axis counterclockwise by 90° in the $x-o-y$ plane, and the $z-$axis is perpendicular to the $x-o-y$ plane following the right-hand rule.

The dihedral angles φ_{13} and φ_{13} give

$$\varphi_{13} = \pi - \arccos\frac{\overrightarrow{N_{I}}\cdot\overrightarrow{N_{III}}}{\left|\overrightarrow{N_{I}}\right|\left|\overrightarrow{N_{III}}\right|}, \quad \varphi_{24} = \pi - \arccos\frac{\overrightarrow{N_{II}}\cdot\overrightarrow{N_{IV}}}{\left|\overrightarrow{N_{II}}\right|\left|\overrightarrow{N_{IV}}\right|}, \tag{A7}$$

where the "$\pi -$" is added because the two normal vectors both pointing inside or outside of the dihedral angle. The folding angles θ_i $(i=1,2,3,4)$ are defined as the dihedral angles between the facets and the auxiliary plane III or IV [Fig. A1], which can be obtained similarly through vector dot products

$$\theta_1 = \arccos\frac{\overrightarrow{N_{1}}\cdot\overrightarrow{N_{III}}}{\left|\overrightarrow{N_{1}}\right|\left|\overrightarrow{N_{III}}\right|}, \quad \theta_2 = \arccos\frac{\overrightarrow{N_{2}}\cdot\overrightarrow{N_{III}}}{\left|\overrightarrow{N_{2}}\right|\left|\overrightarrow{N_{III}}\right|}, \quad \theta_3 = \pi - \arccos\frac{\overrightarrow{N_{3}}\cdot\overrightarrow{N_{IV}}}{\left|\overrightarrow{N_{3}}\right|\left|\overrightarrow{N_{IV}}\right|}, \quad \theta_4 = \pi - \arccos\frac{\overrightarrow{N_{4}}\cdot\overrightarrow{N_{IV}}}{\left|\overrightarrow{N_{4}}\right|\left|\overrightarrow{N_{IV}}\right|}, \tag{A8}$$

We remark that the rectangular coordinate can be built in other ways, through coordinate translations and rotations. However, expressions for these geometry quantities do not depend on the coordinate systems because they are calculated based on the relative relations among vectors. We also remark that the above expressions work for all the four types of cell in this study. Taking a step of $h_{\rho_1} = 0.5^{\circ}$ to traverse $[0^{\circ}, 180^{\circ}]$, plots of L, W, D, φ_S, φ_{13} and φ_{24} with respect to ρ_1 (i.e., Fig. 1(c)~(f)) can be obtained.

Appendix B. Analytical expressions for the geometry quantities in GFF and SC cells

Due to the flat-foldability and collinearity, geometries of the GFF and SC cells are significantly simplified and can be explicitly expressed, which makes it easier to find the conditions for stacking two cells together and to calculate the Poisson's ratios. Here we display the expressions for the geometry quantities.

For GFF and SC cells, φ_{13} always coincides with φ_{24} or $(180^\circ - \varphi_{24})$ [see Fig. 1(e)], indicating that the auxiliary planes III and IV in Fig. A1 are coplanar (no bending deformation). Hence, during folding, the vertices V_2, V_4, V_5, V_6, V_7 and V_8 always stay on the same auxiliary plane, i.e., the $x-o-y$ plane [Fig. B1, B2]. Meanwhile, since V_0V_3 and V_0V_1 are parallel to the $x-o-y$ plane, vertices V_0, V_1, and V_3 stay on a plane parallel to the $x-o-y$ plane. Then the distances from the vertices V_0, V_1, and V_3 to the $x-o-y$ plane are the same, which induces an important identical relation:

$$\sin\alpha_i \sin\theta_i = \text{const}, \quad (i = 1,...,4), \tag{B1}$$

where for the GFF cell, $\alpha_1 = \alpha$, $\alpha_2 = \pi - \beta$, $\alpha_3 = \pi - \alpha$, $\alpha_4 = \beta$; and for the SC cell, $\alpha_1 = \alpha$, $\alpha_2 = \pi - a$, $\alpha_3 = \pi - \beta$, $\alpha_4 = \beta$.

Geometries of the GFF cell. In the GFF cell (with dimensions a, b , and sector angles α, β $(\alpha<\beta)$) [Fig. B1], the dihedral angles ρ_i $(i = 2,3,4)$ can be expressed as functions of ρ_1 based on spherical trigonometry, i.e.,

$$\begin{aligned}
\rho_2 &= \arccos\left(\frac{\cos\alpha + \cos\beta\cos\xi}{\sin\beta\sin\xi}\right) + \arccos\left(\frac{\cos\beta + \cos\alpha\cos\xi}{\sin\alpha\sin\xi}\right), \\
\rho_3 &= \rho_1, \\
\rho_4 &= \arccos\left(\frac{-\cos\alpha - \cos\beta\cos\xi}{\sin\beta\sin\xi}\right) + \arccos\left(\frac{-\cos\beta - \cos\alpha\cos\xi}{\sin\alpha\sin\xi}\right),
\end{aligned} \tag{B2}$$

where $\xi = \arccos\left(-\cos\alpha\cos\beta + \sin\alpha\sin\beta\cos\rho_1\right)$. At the initial stage of folding, ρ_1 begins to decrease from 180°; and all the folding angles θ_i $(i = 1,...,4)$ are acute angles, which can be expressed as

$$\begin{aligned}
\theta_1 = \theta_3 &= \arcsin\frac{\sqrt{2}\sin\beta\sin\rho_1}{\sqrt{2 - \cos(2\alpha) - \cos(2\beta) - 4\sin\alpha\sin\beta\cos\rho_1}}, \\
\theta_2 = \theta_4 &= \arcsin\frac{\sqrt{2}\sin\alpha\sin\rho_1}{\sqrt{2 - \cos(2\alpha) - \cos(2\beta) - 4\sin\alpha\sin\beta\cos\rho_1}}.
\end{aligned} \tag{B3}$$

During folding, θ_i $(i = 1,2,3,4)$ increases with the decrease of ρ_1. Since $\alpha < \beta$, θ_1 and θ_3 will reach 90° prior to θ_2 and θ_4. The critical value of ρ_1 (say, ρ_{1C}) corresponding to the instant that θ_1 and θ_3 reach 90° [Fig. B1(b)] can be determined by solving the equation $\theta_1 = \theta_3 = 90^\circ$. After the critical point, θ_1 and θ_3 become obtuse angles and keep increasing [Fig. B1(c)], while θ_2 and θ_4 remain acute angles and decrease. The expressions for the folding angles after the critical point (denoted by the subscript '$_C$') yield

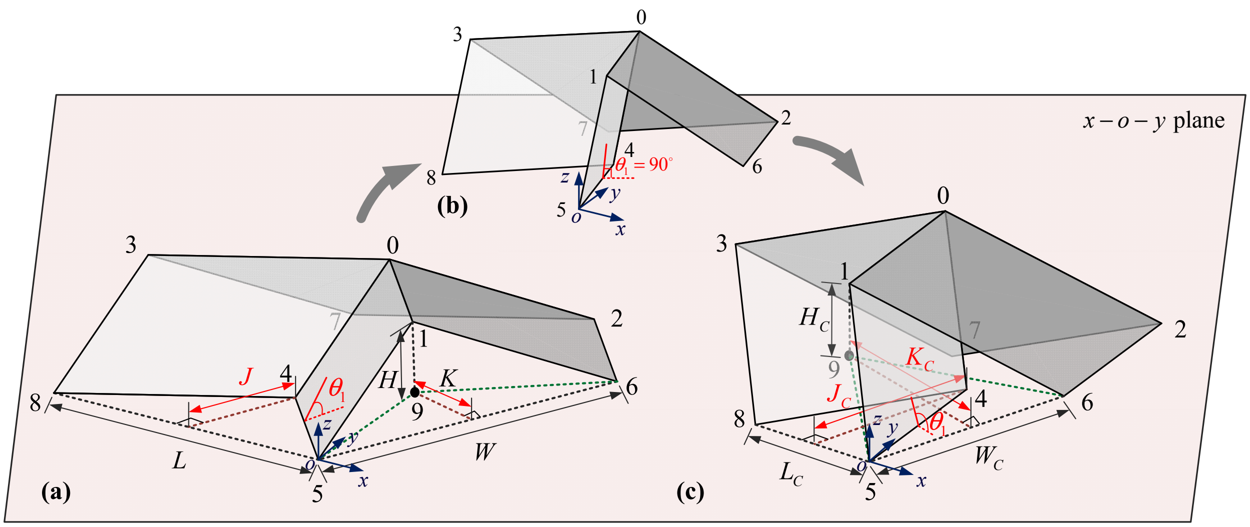

FIG. B1. Geometry of the GFF cell (with dimensions a, b, and sector angles α, β ($\alpha<\beta$)). Partly folded states of the cell are shown: (a) before the critical point ($\theta_1=\theta_3=90^\circ$), (b) at the critical point, and (c) after the critical point. During folding, the vertices V_2, V_4, V_5, V_6, V_7, and V_8 always locate on the $x-o-y$ plane.

$$\begin{aligned}\theta_{1C}=\theta_{3C}&=\pi-\arcsin\frac{\sqrt{2}\sin\beta\sin\rho_1}{\sqrt{2-\cos(2\alpha)-\cos(2\beta)-4\sin\alpha\sin\beta\cos\rho_1}},\\ \theta_{2C}=\theta_{4C}&=\arcsin\frac{\sqrt{2}\sin\alpha\sin\rho_1}{\sqrt{2-\cos(2\alpha)-\cos(2\beta)-4\sin\alpha\sin\beta\cos\rho_1}}.\end{aligned}\tag{B4}$$

Based on the above dihedral angles ρ_i and folding angles θ_i, θ_{iC}, the length L, width W, and height H can be obtained. Before the critical point, we have

$$\begin{aligned}L&=2b\sin\left(\frac{1}{2}\left(\arccos\frac{\cos\alpha}{\sqrt{1-\sin^2\alpha\sin^2\theta_1}}+\arccos\frac{\cos\beta}{\sqrt{1-\sin^2\beta\sin^2\theta_4}}\right)\right),\\ W&=2a\sqrt{1-\sin^2\alpha\sin^2\theta_1}\,\sin\left(\frac{1}{2}\left(\arccos\frac{\cos\alpha}{\sqrt{1-\sin^2\alpha\sin^2\theta_1}}+\arccos\frac{-\cos\beta}{\sqrt{1-\sin^2\beta\sin^2\theta_4}}\right)\right),\\ H&=a\sin\alpha_i\sin\theta_i\ \ (i=1,2,3,4);\end{aligned}\tag{B5}$$

and after the critical point, we have

$$\begin{aligned}L_C&=2b\sin\left(\frac{1}{2}\left(-\arccos\frac{\cos\alpha}{\sqrt{1-\sin^2\alpha\sin^2\theta_1}}+\arccos\frac{\cos\beta}{\sqrt{1-\sin^2\beta\sin^2\theta_4}}\right)\right),\\ W_C&=2a\sqrt{1-\sin^2\alpha\sin^2\theta_1}\,\sin\left(\frac{1}{2}\left(-\arccos\frac{\cos\alpha}{\sqrt{1-\sin^2\alpha\sin^2\theta_1}}+\arccos\frac{-\cos\beta}{\sqrt{1-\sin^2\beta\sin^2\theta_4}}\right)\right),\\ H_C&=a\sin\alpha_i\sin\theta_i\ \ (i=1,2,3,4).\end{aligned}\tag{B6}$$

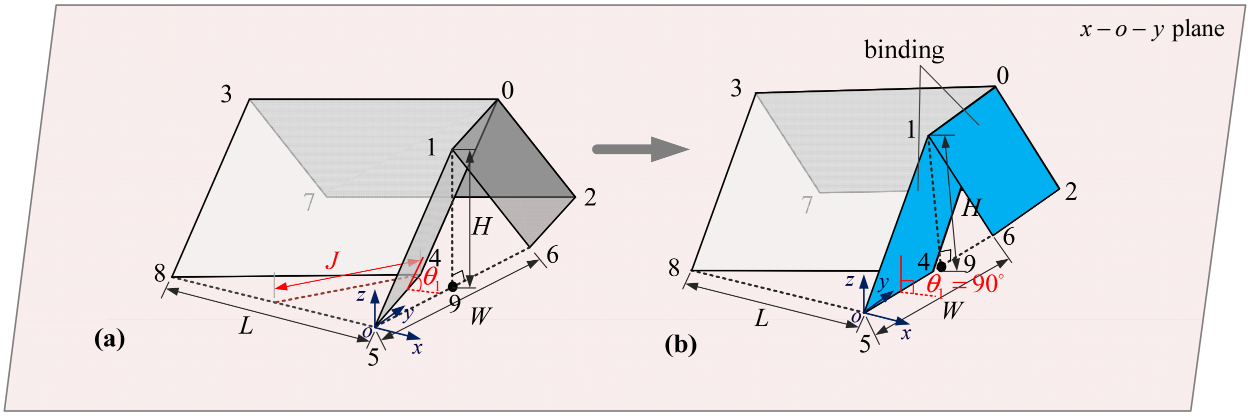

FIG. B2. Geometry of the SC cell (with cell dimensions a, b, and sector angles α, β ($\alpha<\beta$)). (a) Partly folded states of the cell; (b) self-locking state of the cell, where two facets bind together, and $\theta_1=\theta_2=90^{\circ}$. During folding, the vertices V_2, V_4, V_5, V_6, V_7, and V_8 always locate on the $x-o-y$ plane.

We also calculate the quantities J and K, which are useful when deriving the conditions for stacking two GFF cells. J is the distance between vertex V_4 and the line V_5V_8. Plot the perpendicular of the $x-o-y$ plane through vertex V_1, which intersects with the plane at point V_9. K is the distance between point V_9 and the line V_5V_6. Before the critical point, we have

$$J=\sqrt{b^2-(L/2)^2},\ \ K=\sqrt{a^2-H^2-(W/2)^2}; \tag{B7}$$

and after the critical point, we have

$$J_C=\sqrt{b^2-(L_C/2)^2},\ \ K_C=\sqrt{a^2-H^2-(W_C/2)^2}. \tag{B8}$$

Geometries of the SC cell. In the SC cell (with cell dimensions a, b, and sector angles α, β ($\alpha<\beta$)) [Fig. B2], the dihedral angles ρ_i $(i=2,3,4)$ can also be expressed as functions of ρ_1 based on spherical trigonometry:

$$\begin{aligned}
\rho_2&=\arccos\left(\cot\alpha\cot\left(\frac{\xi}{2}\right)\right)+\arccos\left(\cot\beta\cot\left(\frac{\xi}{2}\right)\right),\\
\rho_3&=\arccos\left(\frac{\cos^2\beta+\cos\xi}{\sin^2\beta}\right),\\
\rho_4&=\arccos\left(-\cot\alpha\cot\left(\frac{\xi}{2}\right)\right)+\arccos\left(-\cot\beta\cot\left(\frac{\xi}{2}\right)\right),
\end{aligned} \tag{B9}$$

where $\xi=\arccos\left(-\cos^2\alpha+\sin^2\alpha\cos\rho_1\right)$. At the initial folding stage, the folding angles θ_i $(i=1,2,3,4)$ of the SC cell can be simplified into

$$\begin{aligned}
\theta_1&=\theta_2=(\pi-\rho_1)/2,\\
\theta_3&=\theta_4=(\pi-\rho_3)/2.
\end{aligned} \tag{B10}$$

Since $\alpha<\beta$, we have $\rho_3>\rho_1$. Therefore, when $\rho_1=0$, $\rho_3\neq 0$;i.e., although the facets astride ρ_3 have not bound yet, the facets astride ρ_1 already bind together [Fig. B2(b)]. Such facet-binding prevents the cell from further folding. Besides, we notice that the folding angles θ_i $(i=1,...,4)$ will not larger than 90° during the whole folding process $\rho_1 \in [180^\circ, 0^\circ]$.

Expressions for the length L, width W, and height H keep the same as those in Eq. (B5), providing that $\alpha_2 = \pi - a$ for SC cell. The expression for the quantity J remains the same as that in Eq. (B7). However, noticing from Fig. 2(c) that the auxiliary planes I and II are always perpendicular to the planes III and IV (i.e., the $x-o-y$ plane) during folding, i.e., $\varphi_{13} = \varphi_{24} = 90^\circ$, vertex V_9 always locates on the line $\mathrm{V}_5\mathrm{V}_6$, and the quantity K vanishes.

Appendix C. Stacking geometry of the GFF and SC cells

Two GFF or SC cells can be stacked along their zig-zag crease lines into a stacked unit. To make the two different cells kinematically compatible so that they can stay connected along the zig-zag crease lines during folding, the stacking geometry is derived here.

Stacking of GFF cells. To ensure the kinematic compatibility of two GFF cells, the bottom cell A and top cell B must satisfy the following constraints on extrinsic cell geometry:

$$L_A = L_B,\ W_A = W_B,\ J_A = J_B,\ K_A = K_B, \tag{C1}$$

which is equivalent to

$$L_A = L_B,\ W_A = W_B,\ \angle 458_A = \angle 458_B,\ \angle 956_A = \angle 956_B, \tag{C2}$$

see illustrations in Fig. C1(a). If taking α_B as the independent variable of the top cell B, α_B has to be larger than α_A so that the bottom cell A can be either nested into or bulged out from the top cell B. Then the other geometry parameters of the top cell B can be calculated by

$$b_B = b_A,\ \frac{a_A}{a_B} = \frac{\cos\alpha_B}{\cos\alpha_A},\ \frac{\cos\alpha_A}{\cos\alpha_B} = \frac{\cos\beta_A}{\cos\beta_B}. \tag{C3}$$

The folding angle θ_{B1} of top cell B can be expressed as

$$\theta_{B1} = \arcsin\sqrt{\frac{\cos^2\alpha_A + \cos^2\alpha_B\left(\sin^2\alpha_A \sin^2\theta_{A1} - 1\right)}{\sin^2\alpha_B \cos^2\alpha_A}}. \tag{C4}$$

The other folding angles of the top cell B can be obtained based on the identical relation (see Eq. (B1))

$$\sin\alpha_{Bi}\sin\theta_{Bi} = \text{const},\ \ (i=1,...,4), \tag{C5}$$

where $\alpha_{B1} = \alpha_B,\ \alpha_{B2} = \pi - \beta_B,\ \alpha_{B3} = \pi - \alpha_B,\ \alpha_{B4} = \beta_B$.

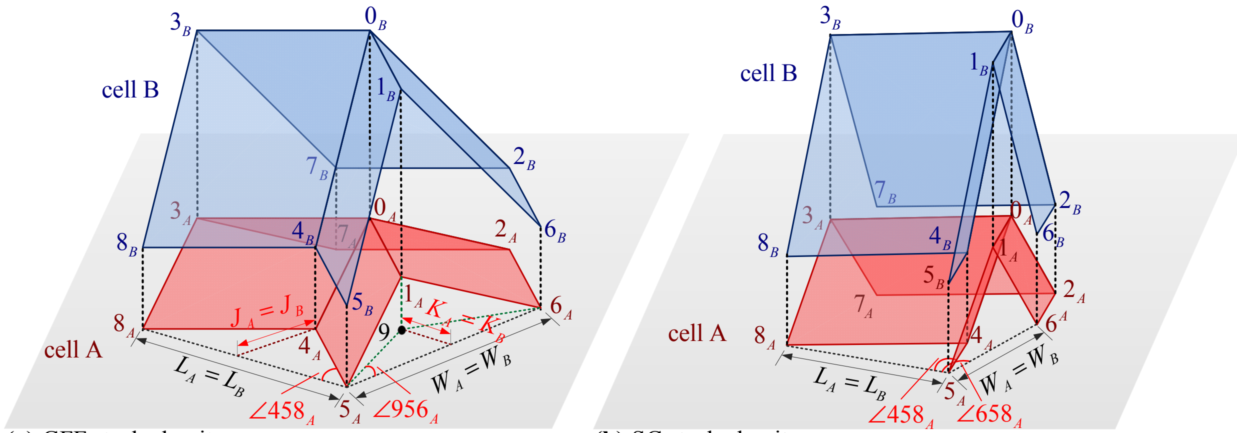

(a) GFF stacked unit **(b)** SC stacked unit

FIG. C1. Illustrations of the stacking conditions for (a) the GFF stacked unit and (b) the SC stacked unit.

Stacking of SC cells. Due to the vanishment of the quantity K, the constraints on extrinsic cell geometry for stacking SC cells are changed to

$$L_A = L_B,\ W_A = W_B,\ \angle 458_A = \angle 458_B,\ \angle 658_A = \angle 658_B, \tag{C6}$$

see the illustrations of angles $\angle 458$ and $\angle 658$ in Fig. C1(b). Similarly, taking $\alpha_B > \alpha_A$ as the independent sector angle, the expressions for the other geometry parameters of the top cell B can be obtained, which remain the same as Eq. (C3). The folding angle θ_{Bi} $(i = 1,...,4)$ of the top cell B can also be calculated by Eq. (C4) and Eq. (C5).

Appendix D. Self-locking in 4-vertex blocks

In addition to the simulation illustrations on self-locking shown in Fig. 3, we provide theoretical analysis on the folding angles to show how self-locking happens in GFF and SC blocks. Fig. D1 (a) and D1(b) show the folding angles ($\theta_{\mathrm{A}i}, \theta_{\mathrm{B}i}$) of the GFF and SC block, respectively. The GFF block has two self-locking states: self-locking of the nested-in configuration is attributed to the binding of bottom-cell facets and top-cell facets (intersection of θ_{A1} and θ_{B1} at 90°, noting that $\theta_{A1} = \theta_{A3}$ and $\theta_{B1} = \theta_{B3}$), which prevents the whole block from further folding; while self-locking of the bulged-out configuration is because that the bottom cell A is folded into a flat state ($\theta_{\mathrm{A1}} = \theta_{\mathrm{A3}} = -180^\circ$, $\theta_{\mathrm{A2}} = \theta_{\mathrm{A4}} = 0^\circ$) and all the four facets bind together, which prevents the whole block from further folding. The SC block also has two self-locking states: at $\rho_{\mathrm{A1}} = 0^\circ$, four facets bind together, two in cell A and two in cell B (θ_{A1}, θ_{A2} and θ_{B1}, θ_{B2} intersect at 90°); at $\rho_{\mathrm{A1}} = 360^\circ$, two facets of cell A (astride ρ_{A1}) and two facets of cell B (astride ρ_{B1}) bind separately (θ_{B1}, θ_{B2} intersect at 90°, while θ_{A1}, θ_{A2} intersect at -90°).

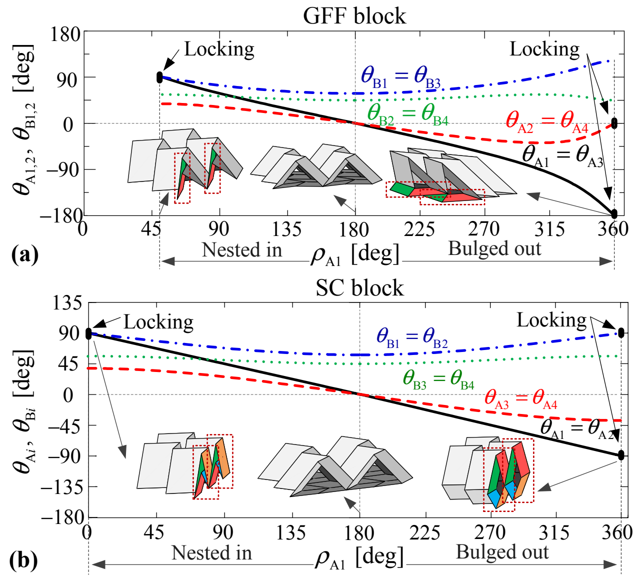

FIG. D1. Self-locking in the stacked GFF and SC blocks. (a) Folding angles of layers A and B in a 2×2×1 GFF block ($a_A = b_A = 1$, $\alpha_A = 36^\circ$ $\beta_A = 72^\circ, \alpha_B = 54^\circ$). (b) Folding angles of layers A and B in the 2×2×1 SC block ($a_A = b_A = 1$, $\alpha_A = 36^\circ, \beta_A = 72^\circ$, $\alpha_B = 54^\circ$). Insets illustrate the configurations of the block at the two locking positions and the transition position ($\rho_{A1} = 180^\circ$). Binding facets are denoted by dotted rectangles.

Appendix E. Poisson's ratio of stacked blocks

In this section, we study the Poisson's ratio in stacked blocks. After stacking multiple stacked units into a block, the height H_S can be expressed as

$$\begin{cases} H_S = n(H_{\mathrm{B}} - H_{\mathrm{A}}) + H_{\mathrm{A}}, & \text{nested in,} \\ H_S = n(H_{\mathrm{B}} + H_{\mathrm{A}}), & \text{bulged out,} \end{cases} \tag{E1}$$

where n is the number of repeating layer pairs AB [Fig. 2], H_{A} and H_{B} are the height of the bottom cell and top cell, respectively. The Poisson's ratio ν_{WL} remains the same as the corresponding sheet; $\nu_{H_S L}$ can be calculated based on Eq. (2) by replacing H with H_S [Fig. E1].

Particularly, we focus on the GFF stacked block and study the effects of the out-of-plane shearing on the Poisson's ratios. The Poisson's ration ν_{WL} remains the same as the GFF sheet, i.e., keeping negative during the whole folding process. However, $\nu_{H_S L}$ shows significant difference with ν_{HL} of the GFF sheet. At the bulged-out configuration, flipping of Poisson's ratio still exists for any n. At the nested-in configuration, when $n = 1$, the structure remains positive $\nu_{H_S L}$; but when $n \geq 2$, $\nu_{H_S L}$ switches to negative. Note that due to self-locking, flipping of $\nu_{H_S L}$ no longer exist in the nested-in configuration. Overall, if the GFF block consists of multiple layer pairs, it can be auxetic in three directions, for both nested-in and bulged-out configurations.

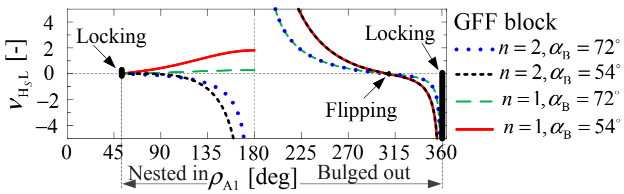

FIG. E1. Poisson's ratio $\nu_{H_S L}$ of the GFF block ($a_A = b_A = 1$, $\alpha_A = 36^\circ, \beta_A = 72^\circ, \alpha_B = 54^\circ$ or 72°, $n = 1$ or 2).

Appendix F. Stiffness in 4-vertex sheets and blocks

Here detailed derivation on the stiffness of the 4-vertex sheets and blocks are provided. In GFF, SC, and Miura-ori sheets, the stretching stiffness along the length and height directions can be expressed through $K_L = \mathrm{d}^2\Pi / \mathrm{d}L^2$ and $K_H = \mathrm{d}^2\Pi / \mathrm{d}H^2$. Through variation principle, we have

$$\begin{aligned} K_L &= \frac{\mathrm{d}^2\Pi}{\mathrm{d}\rho_1^2}\left(\frac{\mathrm{d}L}{\mathrm{d}\rho_1}\right)^{-2} - \frac{\mathrm{d}\Pi}{\mathrm{d}\rho_1}\left(\frac{\mathrm{d}L}{\mathrm{d}\rho_1}\right)^{-3}\frac{\mathrm{d}^2 L}{\mathrm{d}\rho_1^2}, \\ K_H &= \frac{\mathrm{d}^2\Pi}{\mathrm{d}\rho_1^2}\left(\frac{\mathrm{d}H}{\mathrm{d}\rho_1}\right)^{-2} - \frac{\mathrm{d}\Pi}{\mathrm{d}\rho_1}\left(\frac{\mathrm{d}H}{\mathrm{d}\rho_1}\right)^{-3}\frac{\mathrm{d}^2 H}{\mathrm{d}\rho_1^2}. \end{aligned} \tag{F1}$$

Similarly, the shearing stiffness $G_I = \mathrm{d}^2\Pi / \mathrm{d}\varphi_S{}^2$ and $G_O = \mathrm{d}^2\Pi / \mathrm{d}\varphi_{13}{}^2$ can be expressed as

$$\begin{aligned} G_I &= \frac{\mathrm{d}^2\Pi}{\mathrm{d}\rho_1^2}\left(\frac{\mathrm{d}\varphi_S}{\mathrm{d}\rho_1}\right)^{-2} - \frac{\mathrm{d}\Pi}{\mathrm{d}\rho_1}\left(\frac{\mathrm{d}\varphi_S}{\mathrm{d}\rho_1}\right)^{-3}\frac{\mathrm{d}^2 \varphi_S}{\mathrm{d}\rho_1^2}, \\ G_O &= \frac{\mathrm{d}^2\Pi}{\mathrm{d}\rho_1^2}\left(\frac{\mathrm{d}\varphi_{13}}{\mathrm{d}\rho_1}\right)^{-2} - \frac{\mathrm{d}\Pi}{\mathrm{d}\rho_1}\left(\frac{\mathrm{d}\varphi_{13}}{\mathrm{d}\rho_1}\right)^{-3}\frac{\mathrm{d}^2 \varphi_{13}}{\mathrm{d}\rho_1^2}. \end{aligned} \tag{F2}$$

Notice that due to the out-of-plane shearing deformation, the height H and the dihedral angle φ_{13} will experience a switch from increasing to decreasing [Fig. F1(a) and F1 (b)], which as a result induces the stiffness jump and stiffness switch on K_H and G_O, respectively [Fig. F1(c) and F2(d)].

In GFF, SC, and Miura-ori stacked units, the total elastic energy (Π_{Block}) is contributed by three parts: the spring energy stored in the bottom cell A (Π_A), the spring energy stored in the top cell B (Π_B), and the energy stored in the connecting creases (Π_C). Assigning k_A as the linear torsional stiffness per unit length at the creases in cell A, k_B as the linear torsional stiffness per unit length at the creases in cell B, and k_C as the linear torsional stiffness per unit length at the connecting creases, the torsional spring constant K_{Ai} at each crease in in cell A, K_{Bi}

at each crease in cell B, and K_{Ci} at each connecting crease can be accordingly calculated by multiplying k_A, k_B, and k_C with crease length. Then the total energy in stacked units yields

$$\Pi_{\text{Block}} = \Pi_A + \Pi_B + \Pi_C \tag{F3}$$

where

$$\begin{aligned}
\Pi_A &= \frac{1}{2}\sum_{i=1}^{4} K_{Ai}\left(\rho_{Ai} - \rho_{Ai}^0\right)^2, \\
\Pi_B &= \frac{1}{2}\sum_{i=1}^{4} K_{Bi}\left(\rho_{Bi} - \rho_{Bi}^0\right)^2, \\
\Pi_C &= \frac{1}{2}\sum_{i=1}^{4} K_{Ci}\left(\left(\theta_{Bi} - \theta_{Ai}\right) - \left(\theta_{Bi}^0 - \theta_{Ai}^0\right)\right)^2.
\end{aligned} \tag{F4}$$

Since the dihedral angles and folding angles of both cells have been obtained in Appendix A, the stretching stiffness and shearing stiffness of the blocks can be similarly obtained through variation principle. However, it should be noted that in stacked blocks, the geometry parameters that served as the differential variables may be different with those in sheets, and call for re-definition.

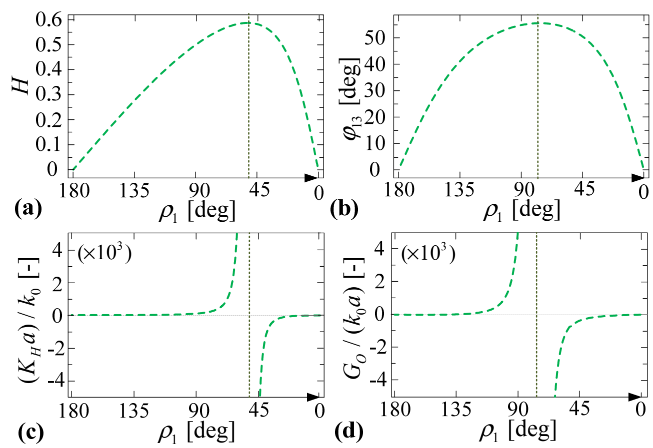

FIG. F1. In the GFF sheet ($a = b = 1$, $\alpha = 36^\circ, \beta = 72^\circ$), the (a) height H, (b) angle φ_{13}, (c) normalized stretching stiffness $(K_H a)/k_0$, and (d) normalized shearing stiffness $G_O/(k_0 a)$ with respect to the folding process. Switches on the geometry quantities and the normalized stiffness are denoted by the dotted vertical lines.

REFERENCE

[1] M. Schenk and S. D. Guest, Proc. Natl. Acad. Sci. **110**, 3276 (2013).
[2] C. Lv, D. Krishnaraju, G. Konjevod, H. Yu, and H. Jiang, Sci. Rep. **4**, 5979 (2014).
[3] E. T. Filipov, T. Tachi, and G. H. Paulino, Proc. Natl. Acad. Sci. 201509465 (2015).
[4] J. L. Silverberg, A. A. Evans, L. McLeod, R. C. Hayward, T. Hull, C. D. Santangelo, and I. Cohen, Science (80-.). **345**, 647 (2014).
[5] H. Yasuda and J. Yang, Phys. Rev. Lett. **114**, 185502 (2015).
[6] J. T. B. Overvelde, T. A. De Jong, Y. Shevchenko, S. A. Becerra, G. M. Whitesides, J. C. Weaver, C. Hoberman, and K. Bertoldi, Nat. Commun. **7**, 10929 (2016).
[7] J. L. Silverberg, J. Na, A. A. Evans, B. Liu, T. C. Hull, C. D. Santangelo, R. J. Lang, R. C. Hayward, and I. Cohen, Nat. Mater. **14**, 389 (2015).
[8] Z. Y. Wei, Z. V. Guo, L. Dudte, H. Y. Liang, and L. Mahadevan, Phys. Rev. Lett. **110**, 215501 (2013).
[9] S. Li and K. W. Wang, Smart Mater. Struct. **24**, 105031 (2015).
[10] S. Li and K. W. Wang, in *Proc. SPIE 9431, Act. Passiv. Smart Struct. Integr. Syst. 2015* (2015), p. 94310H.
[11] B. H. Hanna, J. M. Lund, R. J. Lang, S. P. Magleby, and L. L. Howell, Smart Mater. Struct. **23**, 94009 (2014).
[12] S. Li and K. W. Wang, J. R. Soc. Interface **12**, 20150639 (2015).
[13] S. Waitukaitis, R. Menaut, B. G. Chen, and M. van Hecke, Phys. Rev. Lett. **114**, 55503 (2015).
[14] F. Lechenault and M. Adda-Bedia, Phys. Rev. Lett. **115**, 235501 (2015).
[15] N. Turner, B. Goodwine, and M. Sen, Proc. Inst. Mech. Eng. Part C J. Mech. Eng. Sci. 954406215597713 (2015).
[16] A. Lebée, Int. J. Sp. Struct. **30**, 55 (2015).
[17] E. A. Peraza-Hernandez, D. J. Hartl, R. J. Malak Jr, and D. C. Lagoudas, Smart Mater. Struct. **23**, 94001 (2014).
[18] M. Schenk, A. D. Viquerat, K. a. Seffen, and S. D. Guest, J. Spacecr. Rockets **51**, 762 (2014).
[19] S. Waitukaitis and M. van Hecke, Phys. Rev. E **93**, 23003 (2016).
[20] T. Hull, *Project Origami: Activities for Exploring Mathematics*, 2nd ed. (CRC Press, Boca Raton, 2013).
[20] See the Supplemental Material at… for video illustrations of the folding processes of the 4-vertex cells, sheets, and blocks.
[21] In the GFF block, the out-of-plane shear is confined in each layer of stacked units, but cannot be accumulated among layers.